Available online at www.sciencedirect.com

jmr&t Journal of Materials Research and Technology

www.jmrt.com.br

Original Article

The influence of carbon nanotube addition on the phase composition, microstructure and mechanical properties of 316L stainless steel consolidated by spark plasma sintering

Péter Jenei[a,*], *Csaba Balázsi*[b], *Ákos Horváth*[b], *Katalin Balázsi*[b], *Jenő Gubicza*[a]

[a] *ELTE Eötvös Loránd University, P.O.B. 32, H-1518 Budapest, Hungary*

[b] *Centre for Energy Research, Hungarian Academy of Sciences, Budapest, Hungary*

ARTICLE INFO

Article history:
Received 27 February 2018
Accepted 11 July 2018
Available online 19 October 2018

Keywords:
Composite
Carbon nanotube
Sintering
Microstructure
Mechanical properties

ABSTRACT

Composites of 316L steel and carbon nanotubes (CNTs) were produced by powder metallurgy using high energy milling and spark plasma sintering. The influence of CNT content on the microstructure and the mechanical properties was studied, therefore in addition to the composite samples containing 1 and 3 wt.% CNTs, a 316L specimen without CNTs was also processed. It was found that the CNT addition resulted in a smaller grain size and a higher dislocation density in the matrix. The fraction of the Fe_3C phase formed due to the CNT addition increased with increasing the CNT content. The smaller grain size, the higher dislocation density and the larger fraction of the Fe_3C phase led to a higher hardness in the samples containing CNTs. At the same time, the strength determined by bending was reduced, most probably due to the weak bonding between the 316L grains and the CNTs.

1. Introduction

316L stainless steel is in the focus of materials science due to its excellent corrosion resistance and tailorable mechanical properties [1–3]. Both the strength and the ductility of 316L steel can be varied in a wide range by changing its phase composition. The γ-austenite with a face-centered cubic (fcc) structure usually has a good ductility while its strength is not very high [4]. This phase can be transformed into a body-centered cubic (bcc) α-phase which exhibits a very high strength but with a very limited ductility. The plastic deformation usually results in a martensitic phase transformation from γ-austenite to α-martensite while a reverse phase transformation may occur during high temperature annealing [5,6]. The desired combination of strength and ductility can be achieved in a multiphase 316L steel where the appropriate ratio of γ- and α-phases is adjusted by thermomechanical treatments. Another strategy to improve the mechanical performance of 316L steel is the addition of secondary phase particles such as carbon nanotubes (CNTs).

CNTs are often used as reinforcing filler materials in different composites [7]. The addition of CNTs to the matrices of polymers, ceramics or metals can increase their hardness

* *Corresponding author.*
E-mail: jenei@metal.elte.hu (P. Jenei).

https://doi.org/10.1016/j.jmrt.2018.07.019

and elastic modulus. Furthermore, CNTs can improve the thermal stability of the fine-grained microstructure in the matrix by impeding recovery and recrystallization during annealing at high temperatures [8]. However, these effects strongly depend on the dispersion of CNTs in the matrix and the strength of the bonds between CNTs and the matrix grains [9]. The agglomeration of nanotubes usually hinders their uniform dispersion in the matrix, and the CNT clusters impede the development of strong metal–metal bonds between the matrix grains. As a consequence, the resistance of the materials against the crack propagation may decrease, resulting in lower toughness and strength values. In addition, the elastic modulus of the composite may also be lower than that for the pure matrix material [10]. Therefore, in order to achieve a sufficient dispersion of CNTs, the blend of matrix powder and CNTs is often processed by high-energy milling and then the composite powder is sintered by spark plasma sintering (SPS) [10,11]. SPS results in a full densification of specimens at lower temperatures and holding times (e.g., at 900 °C for 5 min) compared to conventional sintering processes such as hot pressing or hot isostatic pressing [11]. This technique has a high potential to process bulk composites with strong inter-particle bonding. A high degree of dispersion of CNTs in the matrix can be achieved by the treatment of CNTs using surfactants [12] or by the functionalization of nanotubes [13].

In the recent years, several studies were published on steel-CNT composites. Fe-Cr-CNTs nanocomposite feedstock powders were produced by chemical vapour deposition and successfully applied as thermal spray coatings [14,15]. The CNTs were in situ grown without catalyst directly on Fe-Cr feedstock powder surface with an optimal synthesis condition which assured a homogeneous and uniform distribution of CNTs. The as prepared Fe-Cr-CNTs feedstock powders were used to produce wear and corrosion resistant thick coatings by Low Velocity Oxy-Fuel (LVOF) spraying. Fe-CNT nanocomposites with CNT contents between 0.5 and 1 wt.% were successfully manufactured by ball milling and a subsequent SPS-processing at 950 °C for 5 min [15]. It is expected that these Fe-CNT composites could be possible candidates for metallic stents due to its low biodegradability and satisfactory mechanical properties. These materials exhibit a low corrosion rate and slightly enhanced yield and ultimate compression strength without any cytotoxicity. Ultrasonic agitation before milling was found to be an effective way of dispersing CNTs in Fe-Co matrices and the iron-oxide layer developed during milling decreased the temperature required for SPS sintering [16]. Although numerous iron-based CNT composites were investigated in the literature, to the knowledge of the authors no study was published on sintered 316L-CNT composites.

In this paper, the influence of CNT addition on the microstructure and the mechanical properties of 316L steel is studied. The samples were sintered from the blends of 316L powder and CNTs using SPS method. The blend of the 316L steel powder and the CNTs was homogenized by high energy milling. The CNT content of the specimens varies between zero and 3 wt.%. The microstructure and the phase composition of the initial powders and the sintered materials are investigated by X-ray diffraction (XRD) and scanning electron microscopy (SEM). To the knowledge of the authors, this is the first study in the literature which investigates the effect of CNTs on the dislocation density formed during processing of 316L-based composites by powder metallurgy. The correlation between the microstructure and the mechanical performance is discussed in detail.

2. Experimental

2.1. *Sample preparation*

The samples were processed from a commercial 316L austenitic stainless steel powder (manufacturer: Höganäs) with the composition of Fe–16.8% Cr–12% Ni–2.5% Mo–1.5% Mn–0.6% Si (wt.%). The disperse phase in the composites was multiwalled carbon nanotubes (MWCNTs) (manufacturer: Nanocyl, Belgium) with 5 nm in thickness and several tens of micrometer in length. First, the starting 316L powder was intensively milled in DMQ-07 attritor (manufacturer: Union Process) at 2800 rpm for 10 h in propanol. In this machine, a stainless steel setup with delta disk agitators were used. The diameters of the stainless steel grinding balls were 1 mm. After sieving in a 100 μm mesh, the powder was milled in a dry environment for 1 h at 600 rpm in 01-HD/HDDM type attritor. After this milling process, 1 and 3 wt.% MWCNTs were added to the 316L powder and this powder blend was further milled in the 01-HD/HDDM type attritor equipped with stainless steel tank, delta disk agitators and grinding media with 1 mm in diameter. The high energy milling was performed at 4000 rpm for 3 h in ethanol in order to achieve an efficient dispersion of the carbon nanotubes in the commercial 316L powder. Finally, the milled powders were sieved in a 100 μm mesh. A reference 316L powder was also processed without the addition of MWCNTs. However, this powder was subjected to the same milling process as the blends of 316L powder and MWCNTs.

The powders were sintered by SPS in a vacuum at 900 ± 10 °C for 5 min under a pressure of 50 MPa. SPS-processing was carried out by an SPS-7.40MK-VII machine (manufacturer: SPS Syntex Inc.) installed in Istanbul Technical University using a current of 20,000 A. Disks with 50 mm in diameter and 5 mm in thickness were obtained after the consolidation process. In the following, the samples processed from pure 316L, the blend of 316L and 1 and 3 wt.% MWCNTs are denoted as 316L, 316L-1CNT and 316L-3CNT, respectively.

2.2. *Microstructure investigation*

The mass density of the consolidated samples was measured in water using Archimedes' principle. The phase composition and the microstructure of the samples were studied by XRD, SEM and electron backscattered diffraction (EBSD) techniques. The phase composition of the samples was investigated by a Philips Xpert (radiation wavelength, $\lambda = 0.15418$ nm), X-ray powder diffractometer. The microstructure of the main γ-phase was studied by X-ray line profile analysis (XLPA).

Table 1 – The measured and calculated densities, as well as the porosity of the samples.

Composition	Measured density [g/cm^3]	Calculated density [g/cm^3]	Porosity [%]
316L	7.56 ± 0.08	7.99	5.4 ± 0.1
316L-1CNT	7.48 ± 0.08	7.77	3.8 ± 0.1
316L-3CNT	7.03 ± 0.07	7.37	4.6 ± 0.1

Table 2 – The fractions of the integrated intensities in the XRD patterns for the different phases in the milled 316L powder sample and the specimens sintered with or without CNTs.

Composition	γ-phase	α-phase	Fe_3O_4	$Cr_{23}C_6$	Fe_3C
316L powder	0.73 ± 0.03	0.27 ± 0.03	n.a.	n.a.	n.a.
316L	0.81 ± 0.05	0.14 ± 0.02	0.04 ± 0.01	0.01 ± 0.01	n.a.
316L-1CNT	0.80 ± 0.05	0.10 ± 0.02	0.07 ± 0.02	0.03 ± 0.01	0.04 ± 0.02
316L-3CNT	0.68 ± 0.05	0.13 ± 0.02	0.03 ± 0.01	0.001 ± 0.001	0.16 ± 0.02

The X-ray line profiles were measured by a high-resolution diffractometer using Co $K\alpha_1$ ($\lambda = 0.17889$ nm) radiation. For this measurement the samples were electropolished in an A8 electrolytic solution at RT and a fixed voltage of 10 V for 30 s. Two-dimensional imaging plates detected the Debye–Scherrer diffraction rings. The line profiles were determined as the intensity distribution perpendicular to the rings. The line profiles were evaluated by the convolutional multiple whole profile (CMWP) fitting method [17,18]. In this analysis, the experimental pattern is fitted by the convolution of the instrumental pattern and the theoretical size and strain line profiles. The instrumental pattern was measured on a LaB_6 line profile standard material. The theoretical profile functions used in this fitting procedure are calculated on the basis of a model of the microstructure, where the crystallites have spherical shape and log-normal size distribution, and the lattice strains are assumed to be caused by dislocations. The morphology of the powders was studied by a Zeiss-SMT LEO 1540 XB SEM. The EBSD analysis on the sintered samples was performed using an FEI Quanta 3D dual beam SEM equipped with an EDAX type EBSD system. In order to obtain high-quality EBSD images, the surface of the sample was mechanically polished with the following steps: P1000, P2500, P4000, 1 μm ALOX, Mastermet2 suspension (20 nm silica, manufactured by Buehler). The grain size was determined from the EBSD scans using OIM software (version 5.3) from TexSEM Laboratories.

2.3. *Mechanical tests*

The Vickers hardness of the samples was measured on the electropolished surfaces using a Zwick Roell ZHμ Vickers indenter with an applied load of 300 g and a dwell time of 10 s. The bending strength was determined by three-point bending test with a span of 20 mm using an Instron 1112 tensile/loading machine at room temperature (RT). The bending test was carried out on rectangular bars with a cross-section of 4 mm × 4 mm which were cut from the sintered specimens using a water-jet cutting process. The bending strength was determined on 7–8 samples for each composition.

3. Results

3.1. *Porosity and phase composition*

Table 1 shows the measured densities for the sintered 316L, 316L-1CNT and 316L-3CNT samples. These data were compared with the calculated values determined as the average of the theoretical densities of 316L (7.99 g/cm^3) and MWCNTs (2.1 g/cm^3) weighted by their mass fractions. Then, the porosity was calculated from the deviation of the measured densities from the calculated values, and listed in Table 1. Only slight differences were observed between the porosities of the different samples, and their values varied in the range of ~3.8–5.4%.

The XRD investigations showed that the milled 316L powder before sintering (hereafter referred to as initial powder) consists of an fcc γ-austenite (PDF: 33-0397) and a bcc α-phase (PDF: 06-0696). The phase composition was characterized by the fractions of the integrated intensities for the different phases in the X-ray diffractograms. These intensities are listed in Table 2 for all samples. It is noted that the intensity fractions of the phases are not equivalent to their volume fractions. In the initial powder, the fractions of γ-austenite and α-phase were 0.73 and 0.27, respectively (see Table 2). The addition of CNTs to the 316L powder did not influence the phase composition of the powder obtained after milling. As an example, Fig. 1a shows the XRD pattern for the powder 316L-3CNT. The phase composition of the sintered samples were also studied by XRD and are listed in Table 2. For all sintered specimens, the main phase was γ-austenite with the fraction between 0.68 and 0.81 but α-phase, Fe_3O_4 (PDF: 02-1035) and $Cr_{23}C_6$ (PDF: 14-0704) phases were also identified. The XRD patterns obtained for the sintered 316L, 316L-1CNT and 316L-3CNT samples are shown in Figs. 1b, c and d, respectively. It can be seen that in the samples containing CNTs, a crystalline Fe_3C phase (PDF: 35-0772) was also formed during sintering and the increase of the CNT content yielded a higher fraction of Fe_3C (see Table 2).

3.2. *Microstructure from SEM and EBSD*

Fig. 2a shows the microstructure of the initial 316L powder. The milling process resulted in the formation of thin flakes,

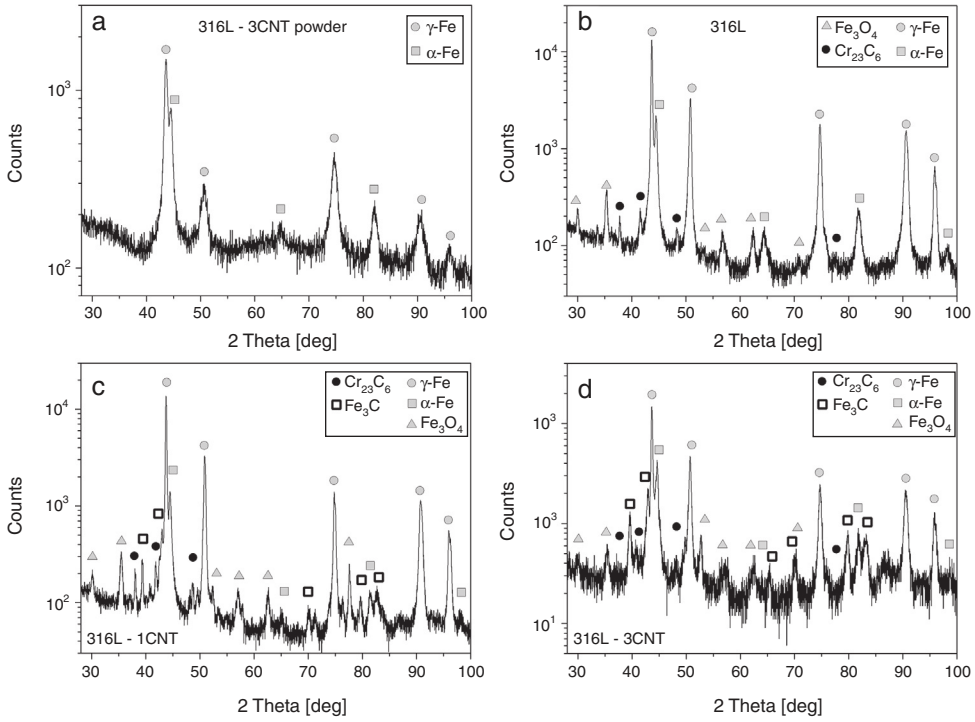

Fig. 1 – X-ray diffractograms for (a) the initial 316L-3CNT powder blend, (b) the sintered 316L, (c) 316L-1CNT and (d) 316L-3CNT samples.

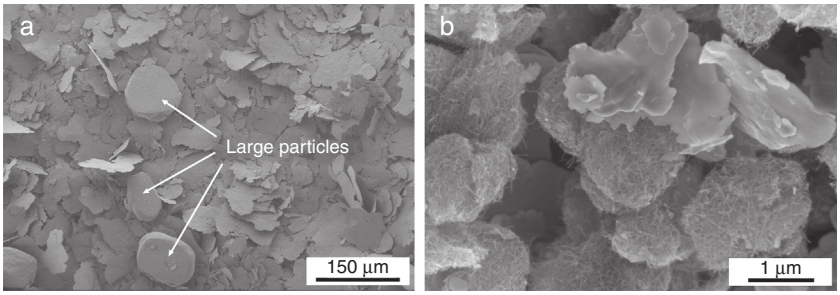

Fig. 2 – SEM images taken on (a) the initial 316L powder and (b) the 316L-3CNT powder blend obtained by milling.

although large thick particles with the diameters of about 100 μm were also detected as indicated by the white arrows in Fig. 2a. The milling of the blend of the 316L powder and the CNTs yielded a dispersion of the carbon nanotube additives as shown in Fig. 2b.

The SEM investigations of the polished surfaces of the sintered samples revealed a heterogeneous microstructure. As an example, Fig. 3a shows a SEM image of the microstructure for the sample 316L-1CNT where light large particles are embedded in a dark matrix. The length and the width of these large particles are about 100 and 30 μm, respectively. The dimensions of these particles suggest that they most probably correspond to the large particles in the initial powder (see Fig. 2a). The EBSD images in Fig. 4 show the grain structure in the sintered specimens 316L, 316L-1CNT and 316L-3CNT. The black areas indicate regions where the grain size could not be detected due to its very small values. Such regions are shown for the sample 316L-3CNT by the white arrows in the SEM image in Fig. 3b. These regions were excluded from the determination of the average grain size. EBSD revealed that the large particles were also fragmented into grains. The average grain sizes obtained for the sintered samples 316L, 316L-1CNT and 316L-3CNT are listed in Table 3. These values represent the average grain sizes for the whole materials containing the different phases. The grain size decreased from ~1.2 to ~0.22 μm due to the addition of 1 wt.% CNTs (see Table 3). The increase of the CNT content from 1 to 3 wt.% did not yield additional grain refinement.

Table 3 – The grain size values for the sintered samples determined by EBSD.

Sample	Grain size [μm]
316L	1.2
316L-1CNT	0.22
316L-3CNT	0.26

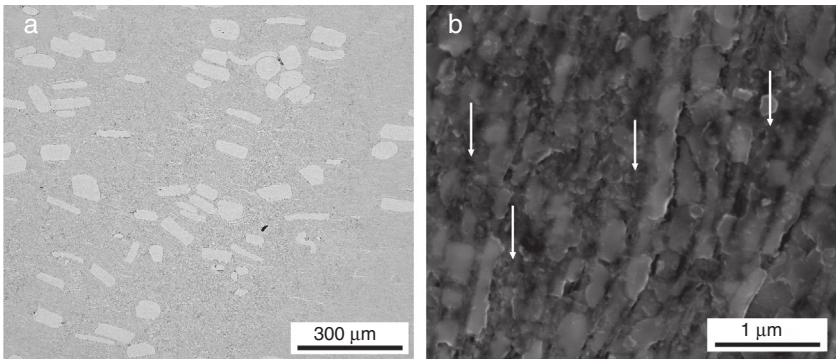

Fig. 3 – (a) SEM image taken on the mechanically polished surface of the sintered sample 316L-3CNT. (b) SEM image with a higher magnification taken on the electropolished surface of 316L-3CNT. The white arrows indicate nanocrystalline volumes which were not evaluated by EBSD due to the very small grain size. These regions are black in the EBSD images of Fig. 4.

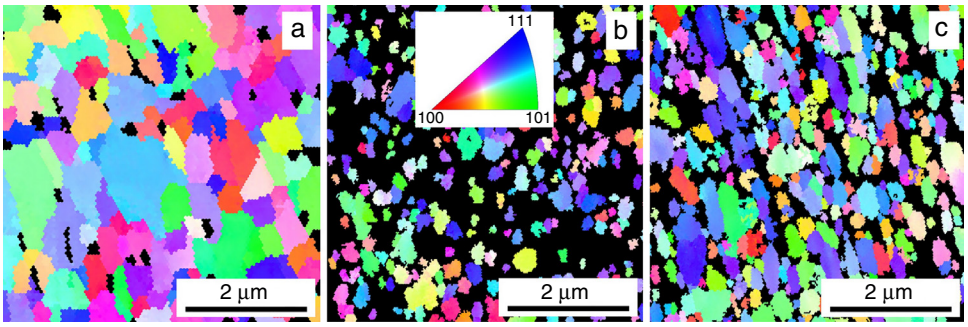

Fig. 4 – Inverse pole figures obtained for the sintered (a) 316L, (b) 316L-1CNT and (c) 316L-3CNT specimens by EBSD.

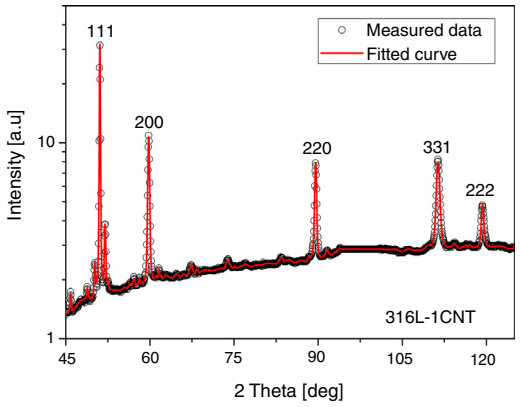

Fig. 5 – CMWP fitting for the X-ray diffraction pattern taken on the sample 316L-1CNT. The open circles and the red solid line represent the measured data and the fitted curves, respectively. The intensity is shown in logarithmic scale. Only the peaks of the γ-austenite phase were evaluated as indicated by the indices of reflections.

3.3. *Crystallite size and dislocation density determined X-ray line profile analysis*

The crystallite size and the dislocation density were determined by XLPA for the initial powder and the sintered samples. As an example, Fig. 5 shows the fitting on the diffractogram measured for the sintered sample 316L-1CNT. The open circles and the solid line represent the measured data and the fitted curves, respectively. As we mentioned in Section 2.2, the diffraction profiles were determined as the intensity distribution perpendicular to the Debye–Scherrer (DS) rings. As an example, Fig. 6a shows the DS ring of reflection *200* for the sintered 316L-3CNT sample. It is noted that only the peaks of the main phase (γ-austenite) were evaluated since the reflections of the other phases were very weak and they strongly overlapped with the high intensity peaks of the γ-phase. In the evaluation, the reflections of the minor phases were put into the background. The area-weighted mean crystallite size and the dislocation density were determined for the γ-phase and listed in Table 4. It should be noted that for the sintered 316L specimen, the intensity distribution along the Debye–Scherrer (DS) rings was inhomogeneous and numerous sharp intensity spots were visible as it can be seen in Fig. 6b. These sharp peaks were as narrow as the instrumental broadening ($\Delta(2\theta) = 0.03^{\circ}$); therefore they were not evaluated for the microstructure. These sharp intensity spots are related to regions in which the crystallite size is larger and the dislocation density is lower than the detection limits of X-ray line profile analysis for the present experimental setup (~800 nm and ~10^{13} m^{-2}, respectively). For the initial powder and the sintered samples 316L-1CNT and 316L-3CNT, only homogeneous intensity distribution was observed in the DS rings.

Due to the spotty diffraction rings for the sintered 316L sample, only the broader and more homogeneous parts

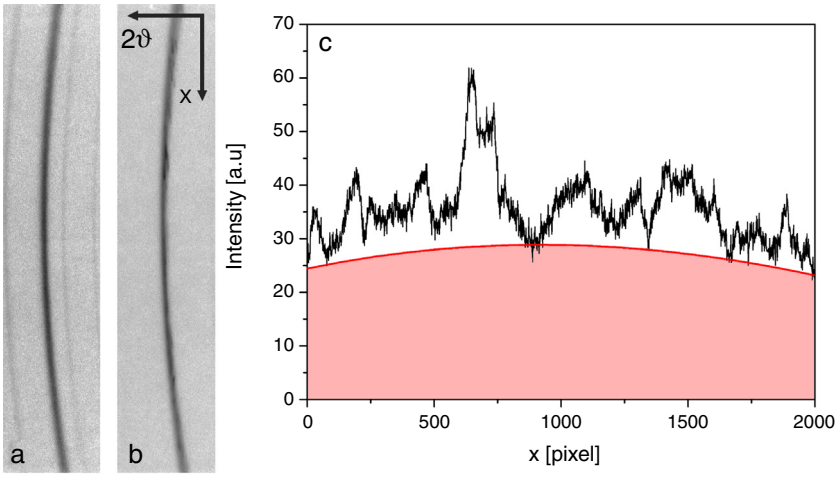

Fig. 6 – Debye–Scherrer diffraction rings of reflection *200* for (a) the 316L-3CNT and (b) the 316L samples. (c) The intensity distribution in direction *x* in figure (b) after subtracting the background. The red zone corresponds to the homogeneous and broad ring segments in (b) scattered from the UFG matrix in the sample.

Table 4 – The dislocation density (ρ_{UFG}) and the average crystallite size ($\langle x\rangle_{UFG}$) obtained by XLPA for the γ-phase in the UFG regions of the materials, and the intensity fraction of these UFG volumes (f_{UFG}). The total dislocation density (ρ_{total}) in the γ-phase was determined as the product of ρ_{UFG} and f_{UFG}.

Sample	$\langle x\rangle_{UFG}$ [nm]	ρ_{UFG} [10^{14} m^{-2}]	f_{UFG}	ρ_{total} [10^{14} m^{-2}]
316L powder	15 ± 2	84 ± 9	1	84 ± 9
316L	95 ± 10	6.3 ± 0.7	0.68 ± 0.05	4.3 ± 0.8
316L + 1% MWCNT	88 ± 14	8.4 ± 0.9	1	8.4 ± 0.9
316L + 3% MWCNT	117 ± 15	8.7 ± 0.9	1	8.7 ± 0.9

between the large intensity spots were evaluated by XLPA. As a consequence, the results obtained for this sample characterize only the ultrafine-grained (UFG) regions of the γ-austenite phase in this specimen (where there are no crystallites with the size higher than ~800 nm). The total dislocation density in the whole γ-austenite can be calculated by considering the coarse grained fractions in the samples. This quantity can be estimated as the fraction of the intensities of the sharp spots in the entire DS ring. The intensity was summed in direction 2θ (see Fig. 6b) after subtracting the background, and these intensity values were plotted as a function of the coordinate x, as shown in Fig. 6c for reflection *200* of the sintered sample 316L. Thereafter, a spline was fitted to the parts of the intensity distribution that are free of sharp intensity peaks (see Fig. 6c). The area under this spline corresponds to the intensity scattered from the UFG parts of the sample. The area under the sharp peaks but above the spline corresponds to the intensity scattered from the coarse grained regions of the γ-austenite phase. From these two quantities, the fraction of the UFG parts (f_{UFG}) for the γ-austenite phase in the sintered 316L sample was determined as 0.68 ± 0.05. For the other two samples, the DS rings were homogeneous, therefore for these samples the microstructural parameters determined by XLPA characterize the whole γ-austenite phase (i.e., the fraction of UFG parts is 100%). In the sintered 316L sample, the dislocation density in the coarse-grained volumes is not higher than ~10^{13} m^{-2} (this is the detection limit), i.e., it is two orders of magnitude smaller then the dislocation density in the UFG regions. Therefore, the total dislocation density for the γ-austenite phase in the sintered 316L sample was calculated as the product of the dislocation density in the UFG regions and their intensity fraction (see Table 4).

Table 4 shows that the initial 316L powder had a very high dislocation density of ~84 × 10^{14} m^{-2} while the crystallite size is as small as ~15 nm. It is noted that the crystallite size measured by XLPA is usually smaller than the grain or particle sizes determined by microscopic methods for severely deformed (e.g., milled) metallic materials. This difference is due to the hierarchical microstructure in the deformed metals where the grains are subdivided into subgrains and/or dislocation cells which scatter X-rays incoherently [19]. Therefore, XLPA measures the size of the subgrains and cells as the crystallite size, also called as the coherently scattering domain size, and this is smaller than the grain size in deformed materials. The very high dislocation density and the small crystallite size in the initial powder can be attributed to the severe plastic deformation occurred during milling. The same values of the crystallite size and the dislocation density were obtained for the powder blends of 316L steel and CNTs as for the 316L powder without CNTs. The sintering at high temperature (900 °C) yielded a strong reduction of the dislocation density and an increase of the crystallite size due to the recovery of the microstructure. The addition of CNTs to 316L steel yielded a two times higher dislocation density while the crystallite size remained practically the same compared to the sintered CNT-free 316L material.

Table 5 – The hardness (HV) and the three-point bending strength for the 316L samples sintered with and without CNTs.

Composition	HV [GPa]	Three-point bending strength [MPa]
316L	3.5 ± 0.2	1324 ± 28
316L-1CNT	4.6 ± 0.4	1237 ± 91
316L-3CNT	5.7 ± 0.5	866 ± 67

3.4. *Mechanical properties*

Table 5 shows the average hardness values obtained for the sintered samples. The addition of 1 wt.% CNTs to 316L steel increased the hardness from 3.5 ± 0.2 to 4.6 ± 0.4 GPa. The increase of the CNT content from 1 to 3 wt.% resulted in an increase of the hardness to 5.7 ± 0.5 GPa. In addition to the hardness, the three-point bending strength values for the sintered samples are also listed in Table 5. It can be seen that the addition of 1 wt.% CNT has no significant effect on the bending strength. At the same time, the bending strength of the 316L-3CNT sample is lower by 35% than the corresponding value for the 316L specimen. The influence of CNTs on the microstructure and the mechanical behavior is discussed in the next section.

4. Discussion

4.1. *The effect of CNT addition on the phase composition and the microstructure of the sintered 316L steel*

The analysis of the phase composition revealed that the sintering of the 316L powder resulted in a decrease of the bcc α-phase fraction from 0.27 to 0.14 (see Table 2). This can be explained by the occurrence of a reverse martensitic phase transformation during high temperature sintering. Most probably, the milling of the 316L powder yielded an increase of the α-phase fraction due to a deformation-induced martensitic phase transformation. Then, the fraction of α-phase was reduced during sintering. Similar phenomenon was observed for the 316L steel samples containing CNTs. In addition, in the sintered materials an Fe_3O_4 phase was detected which was missing from the milled powder, therefore this phase was formed during sintering. Energy-dispersive X-ray spectroscopy (EDS) investigations in SEM (not shown here) revealed that the oxygen content of the powder significantly increased after milling. Then, this oxygen may react with iron forming oxide at the high temperature of sintering. In addition, although SPS was carried out in a vacuum, the oxygen content of the atmosphere in the sample holder may contribute to the formation of an oxide phase.

The addition of CNTs to the 316L powder yielded a formation of Fe_3C (cementite). The carbon content of this phase was most probably supplied by the CNTs and other carbon structures in the powder (e.g., amorphous carbon). The milling of the powder blend of the 316L powder and the CNTs could lead to a fragmentation of the carbon nanostructures and the partial dissolution of these fragments into the heavily distorted microstructure of the 316L steel (mechanical alloying). It is noted that structural defects (e.g., vacancies or Stone-Wales defect [7]) developed in CNTs during milling are preferred sites for this dissolutions. Then, at the high temperature of sintering the majority of lattice defects was annihilated (e.g., the dislocation density decreased by about 90%), therefore the high carbon content was precipitated in a cementite phase. It should be noted that a chemical reaction between the defected carbon nanostructures and the steel matrix may occur at the high temperature of sintering without a preceding carbon dissolution and this reaction may yield the formation of Fe_3C. Reaction between CNTs and metal matrix leading to a carbide formation has already been observed in Ti-CNT composites [20]. For the samples studied in this work, the fraction of the Fe_3C phase increased with increasing the CNT content (see Table 2).

The increase of the crystallite size and the reduction of the dislocation density during sintering indicate that a strong recovery of the milled microstructure occurred at the high temperature of consolidation (see Table 4). The spotty DS rings for the sintered 316L sample suggests that some volume in this specimen were partially recrystallized during consolidation. The addition of CNTs to the powder 316L impeded the recovery and recrystallization of the microstructure during sintering, resulting in a finer microstructure and a higher dislocation density as shown in Tables 3 and 4. This effect may be caused directly by the pinning effect of nanotubes on the grain boundaries and dislocations formed during milling. In addition, the particles of the Fe_3C phase might also increase the stability of the UFG microstructure formed during milling. It is interesting to note that the increase of the CNT content from 1 to 3% did not lead to a higher dislocation density and a smaller grain size. This phenomenon might be caused by the influence of the distribution of CNTs and Fe_3C particles on their effectivity in the retention of recovery and recrystallization. A uniform distribution of CNTs has a stronger hindering effect on defect annihilation compared to a clustered CNT structure. Therefore, even if the CNT content is higher for the sample 316L-3CNT than for the specimen 316L-1CNT, its effect on the recovery and recrystallization during sintering is not stronger most probably due to the high degree of CNT agglomeration. As an example, the SEM image in Fig. 7 shows a CNT cluster on the fracture surface of the sample 316L-3CNT after the

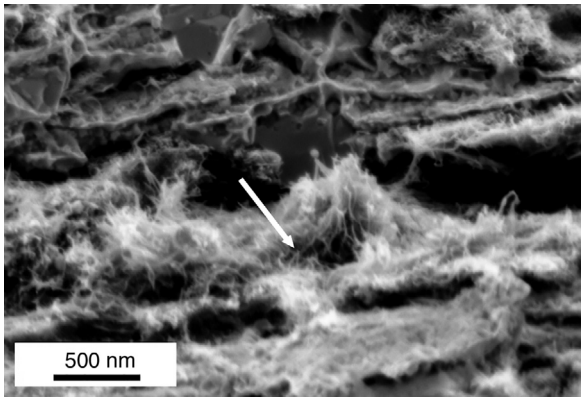

Fig. 7 – SEM image showing the fracture surface of the sample 316L-3CNT after three-point bending test. The arrow indicates an agglomeration of CNTs.

bending test. This image also proves that many CNTs survive the high-energy milling and the sintering by SPS.

4.2. *The influence of CNT addition on the mechanical behavior of the sintered 316L steel*

The main microstructure features which can influence considerably the mechanical properties are (1) the phase composition, (2) the grain size, (3) the dislocation density and (3) the porosity. The latter effect is practically the same for the three sintered materials. The addition of 1% CNTs to the 316L steel yielded an increase in the hardness which can be explained by the smaller grain size, the higher dislocation density and the dispersion strengthening effect of CNTs and Fe_3C particles. The increase of the CNT content from 1 to 3% led to an improvement in the hardness, despite the practically unchanged grain size and dislocation density. Most probably, the dispersion strengthening effect of CNTs and Fe_3C particles was higher for the larger CNT content.

The addition of 1% CNTs did not yield any considerable change in the bending strength. At the same time, a significant decrease in the bending strength was observed for the sample 316L-3CNT (see Table 5). The bending strength was reduced from 1324 ± 28 to 866 ± 67 MPa due to the addition of 3 wt.% CNTs. The lower bending strength can be attributed to the agglomeration of CNTs which weakens the bonding between the 316L grains. It is noted that the clustering of CNTs may be not reflected in the porosity, i.e., the relative density of samples with different distributions of CNTs may be the same. Therefore, the clustering effect of CNTs cannot be taken into account by the measured porosity. The effect of agglomeration of CNTs on the bending strength overwhelms the hardening caused by the CNTs in the studied samples. Indeed, the hardness increased with increasing CNT content due to the effect of the CNTs, the Fe_3C phase, the smaller grain size and the higher dislocation density. However, the weak bonding between the 316L grains yielded a lower failure stress during bending. Therefore, the addition of CNTs into SPS-processed 316L resulted in a harder but less tough material. Further research direction in this field may be to develop new techniques for the improvement of the dispersion of CNTs and their adhesion to the 316L grains. Former studies on other samples (e.g., on Cu-CNT and Al-CNT composites) suggest that molecular level mixing procedures may be a candidate for processing metal-CNT composites with a high level of CNT dispersion [12,13]. However, these methods have been applied only on pure metal matrices while 316L steel comprises of six different constituents (see the composition in Section 2.1). Therefore, the processing methods used successfully for pure matrices must be improved for multicomponent matrix materials.

5. Conclusions

An investigation was conducted to study the effect of CNT addition on the microstructure and the mechanical behavior of 316L steel. Samples with 0, 1 and 3 wt.% of CNTs were sintered by SPS method. The following conclusions were drawn from the experiments:

1. The major phase for all samples was a γ-austenite with the fractions between 0.68 and 0.81. In the sintered CNT-free sample, beside the γ-austenite considerable amounts of bcc α-phase and Fe_3O_4 phase were detected. During sintering at high temperature, the fraction of the α-phase developed during powder milling decreased due to a reverse martensitic transformation. The Fe_3O_4 phase was also formed during the sintering process. The addition of CNTs resulted in the development of an Fe_3C phase. The fraction of this phase increased with increasing the CNT content.
2. Sintering of the 316L powder led to a decrease in the dislocation density and a concomitant increase in the crystallite size due to the recovery and recrystallization of the severely milled microstructure. The addition of CNTs impedes these processes, therefore the dislocation density and the grain size in the 316L-CNT composites were higher and smaller, respectively, than in the CNT-free material. The increase of the CNT content from 1 to 3% did not yield a smaller grain size or a higher dislocation density. Most probably, the clustering of the CNTs in the 316L-3CNT sample decreased the hindering effect of a unit amount of CNTs on recovery and recrystallization.
3. The CNT addition increased the hardness of the sintered 316L alloy due to the hardening effect of the CNTs, the Fe_3C phase, the smaller grain size and the higher dislocation density. At the same time, clustering of CNTs yielded a weaker bonding between the 316L grains, therefore 3% CNT addition resulted in a significant decrease in the bending strength.

Conflicts of interest

The authors declare no conflicts of interest.

Acknowledgments

This research was supported by the Hungarian Scientific Research Fund (OTKA) under grant no. K-109021, National Research, Development and Innovation Office (NKFIH) under grant no. PD-121049 and MTA EK project “Nanostructural ODS steel development”. The authors thank V. Varga for milling the powders, L. Illés for SEM/EDS of the powders and Prof. F.C. Sahin for sintering the samples. JP acknowledges the financial support of the Hungarian Ministry of Human Capacities under Grant no. NTP-NFTÖ-16-0957.

REFERENCES

[1] Chen XH, Lu J, Lu L, Lu K. Tensile properties of a nanocrystalline 316L austenitic stainless steel. Scripta Mater 2005;52:1039–44.
[2] Kim Y, Kim Y, Kim D, Kim S, Nam W, Choe H. Effects of hydrogen diffusion on the mechanical properties of austenite 316L steel at ambient temperature. Mater Trans 2011;52:507–13.
[3] Yan FK, Liu GZ, Tao NR, Lu K. Strength and ductility of 316L austenitic stainless steel strengthened by nano-scale twin bundles. Acta Mater 2012;60:1059–71.

[4] Song R-B, Xiang J-Y, Hou D-P. Characteristics of mechanical properties and microstructure for 316L austenitic stainless steel. J Iron Steel Res Int 2011;18:53–9.
[5] Spencer K, Conlon KT, Bréchet Y, Embury JD. The strain induced martensite transformation in austenitic stainless steels: Part 2 – Effect of internal stresses on mechanical response. Mater Sci Technol 2009;25:18–28.
[6] Nanda T, Kumar BR, Singh V. A thermal cycling route for processing nano-grains in AISI 316L stainless steel for improved tensile deformation behaviour. Defence Sci J 2016;66:529.
[7] Gubicza J. Defect structure and properties of nanomaterials. 2nd and extended edition Duxford, UK: Woodhead Publishing, an imprint of Elsevier; 2017.
[8] Jenei P, Gubicza J, Yoon EY, Kim HS, Lábár JL. High temperature thermal stability of pure copper and copper–carbon nanotube composites consolidated by high pressure torsion. Composites: Part A 2013;51:71–9.
[9] Kim KT, Cha SI, Hong SH, Hong SH. Microstructures and tensile behaviour of carbon nanotube reinforced Cu matrix nanocomposites. Mater Sci Eng A 2006;430:27–33.
[10] Esawi AMK, El Borady MA. Carbon nanotube-reinforced aluminium strips. Compos Sci Technol 2008;68:486–92.
[11] Balázsi C, Gillemot F, Horváth M, Wéber F, Balázsi K, Sahin FC, et al. Preparation and structural investigation of nanostructured oxide dispersed strengthened steels. J Mater Sci 2011;46:4598–605.
[12] Sridhar I, Narayanan KR. Processing and characterization of MWCNT reinforced aluminium matrix composites. J Mater Sci 2009;44:1750–6.
[13] Cha SI, Kim KT, Arshad SN, Mo CB, Hong SH. Extraordinary strengthening effect of carbon nanotubes in metal-matrix nanocomposites processed by molecular-level mixing. Adv Mater 2005;17:1377–81.
[14] Moonngam S, Tunjina P, Deesom D, Banjongprasert C. Fe-Cr/CNTs nanocomposite feedstock powders produced by chemical vapor deposition for thermal spray coatings. Surf Coat Technol A 2016;306:323–7.
[15] Azarniya A, Azarniya A, Hamid Reza SS, Hosseini M, Varol T, Kawasaki A, et al. Physicomechanical properties of spark plasma sintered carbon nanotube-reinforced metal matrix nanocomposites. Progr Mater Sci 2017;90:276–324.
[16] Mani MK, Viola G, Reece MJ, Hall JP, Evans SL. Fabrication of carbon nanotube reinforced iron based magnetic alloy composites by spark plasma sintering. J Alloys Compd 2014;601:146–53.
[17] Ribárik G, Gubicza J, Ungár T. Correlation between strength and microstructure of ball-milled Al–Mg alloys determined by X-ray diffraction. Mater Sci Eng A 2004;387–389: 343–7.
[18] Gubicza J. X-ray Line Profile Analysis in Materials Science. Hershey, PA, USA: IGI-Global; 2014.
[19] Ungár T, Tichy G, Gubicza J, Hellmig RJ. Correlation between subgrains and coherently-scattering-domains. Powder Diffract 2005;20:366–75.
[20] Kuzumaki T, Ujiie O, Ichinose H, Ito K. Mechanical characteristics and preparation of carbon nanotube fiber-reinforced Ti composite. Adv Eng Mater 2000;2: 416–8.